ACS APPLIED ENERGY MATERIALS

Article

MnO2 and Reduced Graphene Oxide as Bifunctional Electro-catalysts for Li-O2 Batteries

Lihua Zhu, Frieder Scheiba, Vanessa Trouillet, Melinte Georgian, Qiang Fu, Angelina Sarapulpva, Florian Sigel, Weibo Hua, and Helmut Ehrenberg

ACS Appl. Energy Mater., **Just Accepted Manuscript** • DOI: 10.1021/acsaem.9b01047 • Publication Date (Web): 06 Sep 2019

MnO_2 and Reduced Graphene Oxide as Bifunctional Electro-catalysts for Li-O_2 Batteries

Lihua Zhu,[†] Frieder Scheiba,[,†] Vanessa Trouillet,[†,§] Melinte Georgian,[‡] Qiang Fu,[†] Angelina Sarapulpva,[†] Florian Sigel,[†] Weibo Hua,[†] and Helmut Ehrenberg[†,‡]*

[†]Institute for Applied Materials -Energy Storage Systems (IAM-ESS), Karlsruhe Institute of Technology (KIT), Hermann-von-Helmholtz-Platz 1, 76344 Eggenstein-Leopoldshafen, Germany.

[‡]Helmholtz-Institute Ulm for Electrochemical Energy Storage (HIU), Helmholtzstrasse 11, 89081 Ulm, Germany.

[§]Karlsruhe Nano Micro Facility, Karlsruhe Institute of Technology, Hermann-von-Helmholtz-Platz 1, 76344, Eggenstein-Leopoldshafen, Germany.

KEYWORDS: rGO, MnO_2, interface, nano-sized, synergistic effect, mass transport, lithiated and non-lithiated, electron transfer.

ABSTRACT

An effective and cheap way to optimize the oxygen electro-catalyst of the cathode for Li-O_2 battery is to control the growth of a low amount of nano-sized transition metal oxides on the surface of the carbon electrode. This approach combines the advantages of surface, interface, and nano-size engineering. In this work, a MnO_2 content of about 9 wt% is deposited on reduced graphene oxide (MnO_2@rGO). The MnO_2 particles grow uniformly on the rGO surface with a particle size smaller than 20 nm. The MnO_2@rGO composites were applied as cathode catalysts in Li-O_2 batteries, demonstrating an initial discharge capacity of 5139 mAh g^{-1} and a high capacity of 4262 mAh g^{-1} (80% capacity retention) after 15 full discharge-charge cycles at a current density of 100 mA g^{-1}. The outstanding performance can be attributed to the strong synergistic effect between the rGO framework and the nano-sized MnO_2 particles on its surface. The rGO framework possesses a porous multilayer structure, which provides an excellent electrical conductivity, promotes oxygen and ion diffusion, and provides storage space for the discharge products. The nano-sized MnO_2 possesses a high exposed surface, which enhances surface transport of LiO_2 species and avoids the accumulation of discharge products on electrode surface. Furthermore, a transition between lithiated and non-lithiated manganese oxide during discharge and charge process was observed. This transition apparently helps to promote electron transfer between discharge products and the catalyst and thereby to reduce the overpotential of the oxygen evolution reaction.

1. INTRODUCTION

Porous air electrodes play different roles in the Li-O_2 battery system: (i) it acts as an active catalyst material for the oxygen reduction/oxygen evolution reaction (ORR/OER).[1] (ii) it serves as conductive framework for electron transfer.[2] (iii) it provides as a matrix to deposit discharge

products.[3,4] (iv) it forms a porous network that supports oxygen diffusion.[5,6] Therefore, it is important to develop suitable oxygen electrode materials to improve the electrochemical performance of Li-O_2 batteries. Intensive research efforts have been devoted to the design and synthesis of appropriate oxygen electrode materials in recent years. Graphene stands out either as a metal-free catalyst or as support for metal or metal oxides catalysts, due to its good electronic conductivity, low cost, and large surface area.[7,8] Due to the limited catalytic effect of pure graphene electrodes to the oxygen reduction reaction and oxygen evolution reaction[9], heteroatom hybridization (N[10], S[11] and B doping), and combination with metals or metal oxides have been widely explored in recent years.[12] Although noble metals (Ru[13], Au[12], Sr[14], Pd[15] and etc.) exhibit decent electrochemical performance toward the ORR and OER, their scarcity and price have doomed them not to be widely used.

Manganese oxides are considered as promising catalysts due to their high abundance, low cost, environmental friendliness and excellent catalytic performance for both ORR and OER.[16-17] Recently, different manganese compounds (α-MnO_2, Mn_3O_4, ε-MnO_2, MnO_x, $MnCoO_4$ and *etc*) with different morphologies and crystalline structures have been reported to have efficient catalytic activity for the OER/ORR of Li-O_2 batteries.[18-19] Metin's group in situ grew one-dimensional (1D) MnO_2 nanowires on 2D mesoporous carbon nitride (MnO_2@mpg-C_3N_4). Benefiting from the effective stabilization of Mn^{3+} species in the electrocatalyst via the help of nitrogen functional groups, MnO_2@mpg-C_3N_4 exhibited a high electrocatalytical efficiency for the OER.[20] Cao's group synthesized α-MnO_2 nanorods on graphene nanosheets (GNs) and applied it as cathode for Li-O_2 battery.[16] The mass percent of α-MnO_2 in the composite is 80%. The battery cycled 25 times with the cut-off capacity of 3000 mAh g^{-1} (based on the mass of GNs). Han et al. reported a MnO_2 composite with hierarchically porous carbon (HPC) through the reaction of $KMnO_4$ and carbon

(90 min at 50°C).[21] The weight percentage of MnO_2 was about 46%. The composite was applied in a Li-O_2 battery, which exhibited low charge overpotential, good rate capacity and long cycle stability up to 300 cycles with a cut-off capacity of 1000 mAh g^{-1}.[21] However, the complex synthesis process of HPC makes it an expensive cathode material. Hwang's team developed an effective chemical way to optimize the electrocatalytical properties of α-MnO_2 nanowire by surface anchoring of highly oxidized selenate (SeO_4^{2-}) clusters.[22] The battery could be cycled 70 times with a cut-off capacity of 1000 mAh g^{-1}. Hwang's team also synthesized holey 2D Mn_2O_3 nanosheets by thermally induced phase transition of exfoliated layered MnO_2 nanosheets.[23] The Li-O_2 battery with holey 2D nanosheets exhibited a cycleability of 33 cycles with a cut-off capacity of 1000 mAh g^{-1}. Bi et al. obtained a 3D hollow α-MnO_2 framework (3D α-MnO_2) by a template-induced hydrothermal reaction and subsequent annealing treatment.[24] A very good cycling stability of 170 cycles with a cut-off capacity of 1000 mA hg^{-1} (33% α-MnO_2 in catalyst material) was obtained with the 3D hollow α-MnO_2 framework catalyzed cathode. Surface morphologies and compositions of materials greatly influence their functional properties. In Li-O_2 batteries, the catalytically active part of the air electrode is its surface.[25] Hence the modification of electrode material surface becomes an efficient and cheap way to enhance the catalytic activity. As we mentioned above, graphene has many advantages when applied as air electrode material for Li-O_2 batteries. However, the low ORR/OER catalytic activity significantly limits its electrochemical performance as air electrode for Li-O_2 batteries. Depositoin of catalysts on the graphene surface provides a way to improve the catalytic activity while preserving the advantages of graphene. Gao et al. reported a facile synchronous reduction strategy to fabricate a yolk-shell Ag-decorated Co_3O_4 (Co_3O_4@Co_3O_4/Ag hybrid).[26] It has been cycled stably for 80 times with the cut-off capacity of 1000 mAh g^{-1}. It has also been reported that nano-sized catalysts can result in more exposed

effective catalytic surface for ORR/OER.[27] Hence loading of nano-sized catalysts on graphene surface can further optimize its catalytic activity.[28]

The combination of transition metal oxides and carbon have been widely explored as the cathode for Li-O_2 battery. However, the detailed catalytic mechanism of the composite is unclear so far. Black's group explored the electrochemical performance of Co_3O_4 grown on reduced graphene oxide (Co_3O_4@RGO) when applied in Li-O_2 battery.[29] They found an improvement of mass transport in both OER and ORR process by Co_3O_4@RGO.

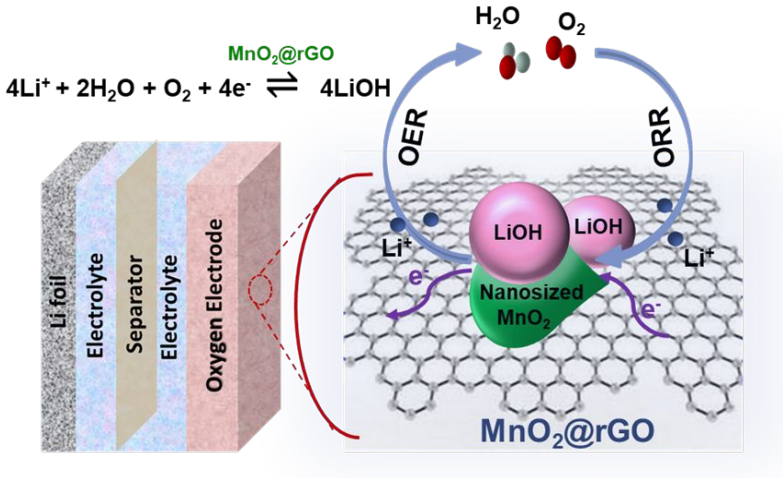

Scheme 1. Schematic structure of Li-O_2 battery catalyzed by MnO_2@rGO. Nanosized MnO_2 uniformly grows in situ on a rGO surface and the composite catalyzes the reversible formation and decomposition of LiOH.

In this work, we assembled a novel kind of MnO_2@rGO nanocomposite material, consisting of a super low amount of nano-sized MnO_2 grains on the surface of rGO (reduced graphene oxide, Dasheng Ltd.), which is highly efficient for the ORR/OER of Li-O_2 batteries (Scheme 1). The MnO_2@rGO composite material is composed of 88 wt% of rGO and 9 wt% MnO_2. We also studied in details the catalytic mechanism of the MnO_2@rGO composite in a Li-O_2 battery. The catalytic mechanism combines the promotion of mass transport of Li_xO_2 species and electron transfer.

2. EXPERIMENTAL

2.1 MnO_2@rGO Material Preparation

MnO_2@rGO was prepared by mixing 100 mg rGO with 500 ml 1mM $KMnO_4$/5 mM Na_2SO_4. The mixture was stirred for 1h. This procedure relies on the chemical reaction between $KMnO_4$ and graphitic carbon to generate MnO_2 ($C+2KMnO_4 \rightarrow K_2MnO_4+MnO_2+CO_2\uparrow$). The multilayer rGO served as reactive template to grow the MnO_2. This constrains the MnO_2 growth rate and thereby the aggregation of MnO_2 nanoparticles is avoided. Na_2SO_4 can increase the solubility of CO_2 in solution and thereby slows down the chemical reaction, which is beneficial to obtain small particles. The obtained suspension was collected by suction filtration and washed with distilled water several times. The resulting product was dried at 80°C for 12 h in the oven.

2.2 Cell Preparation and Eelectrochemical Measurement

The catalyst material was first mixed with PVDF (PVDF6020, Solvay) in N-methyl pyrrolidone (NMP, Merck KGaA) solvent with a mass ratio of 7:3 (MnO_2@rGO:PVDF). Then the slurry was coated on carbon paper (H23 I2, QUINTECH). Li-O_2 cells were assembled using a Swagelok® cell construction. Li-O_2 batteries consisting of a metallic Li foil, a glass fiber separator (Whatmann® GF/B), MnO_2@rGO and the electrolyte were assembled inside an Ar-filled glove box (<0.1 ppm of both oxygen and H_2O). As electrolyte 0.25 M lithium bis(trifluoromethane)-sulfonamide (LiTFSI) in tetra(ethylene) glycol dimethyl ether (TEGDME) was used. According to the Stokes-Einstein equation, lower Li salt concentration of 0.25 M decreases the electrolyte viscosity and thereby increases the oxygen diffusion coefficient. This leads to high oxygen concentration and thereby contributes to a higher discharge capacity and rate capability (the rate-determining step of the oxygen reduction reaction depends first order on the concentration of

oxygen). The gas environment used for the electrochemical test was oxygen with trace water. The determination of the exact amount of water in the gas stream or taken up by the cell during operation was not possible. However, it has been demonstrated by many other research groups that traces of water improve the electrochemical performance of Li-O_2 batteries.[30,31] Electrochemical measurements were carried out on a VSP (Bio-Logic, France) multichannel potentiostat test system at room temperature. Galvanostatic discharge/charge tests were operated at room temperature in the range of 2.3-4.5 V. The cyclic voltammograms (CV) were tested at 0.1 mV s^{-1}. Current densities and specific capacities specified in this paper were calculated based on the total catalyst weight (MnO_2+rGO).

2.3 Characterization of the Raw Materials and the Discharged/Charged Electrodes

SEM (scanning electron microscope, Zeiss Supra 55) was applied to characterize the morphology of the raw catalyst materials and the pristine/discharged/charged electrodes. N_2 adsorption and desorption isotherms were measured with a Micromeritics instrument at 77 K. X-ray diffraction (XRD) patterns of the raw catalyst materials and the pristine/discharged/charged electrodes were examined on STOE STADI P with Ag K_α radiation (λ=0.559407Å) or Co K_α radiation (λ=1.78896 Å) at room temperature in Debye-Scherrer geometry (the capillary diameter: 0.5 mm). XRD with Ag K_α radiation has higher energy and stronger penetration than Co K_α radiation, which makes it superior to analyze structures of metallic compounds. Hence we applied XRD with Ag K_α radiation to analyze the structure of raw catalyst materials. Due to its lower energy Co K_α radiation is more strongly scattered by compounds with low electron density, which makes it superior to analyze the structure of discharge products. Rietveld refinement was employed to analyze the diffraction data of the discharge products using the FullProf software package.[32] The discharged and charged electrodes was disassembled and washed in a glovebox. Then the discharge products were

removed from the electrode surface and filled in a glass capillary (D=0.5 mm) and sealed to avoid air contact during measurement. For Raman measurements, a Labram Evolution HR from Horiba was used, which was equipped with HeNe-Laser (633 nm, 17 mW) and a CCD detector (Horiba). Besides, a 600 grating was used to split the measurement signal. For the raw material, a ×100 objective lens was used for the measurements and the data was collected for 30 seconds with the laser power set to 4.25 mW. For better signal-to-noise ratio, five measurements were added. A ×50 objective lens was used for the measurements of the pristine/discharged/charged electrodes. The data was collected for 60 seconds with the laser power set to 4.25 mW. Again five measurements were added. The discharged and charged electrodes were mounted in a sealed cell with a quartz window inside a glovebox to protect them against air contact. Thermal analysis (TG) of MnO_2@rGO was carried out in air atmosphere with a heating rate of 5 °C min^{-1} to 1000 °C using a Netzsch STA 449 C Jupiter. The surface elemental compositions and oxidation state of elements in the MnO_2@rGO were determined by X-ray photoelectron spectroscopy (XPS). XPS was performed using a K-Alpha spectrometer (ThermoFisher Scientific, East Grinstead, UK) equipped with a microfocused, monochromated Al Kα X-ray source (400μm spot size). A glovebox with argon atmosphere directly attached to the spectrometer enabled an air free insertion of the samples into the load lock. The kinetic energy of the electrons was measured by a 180° hemispherical energy analyzer operated in constant analyzer energy mode (CAE) at 50 eV pass energy for elemental spectra. The K-Alpha charge compensation system was employed during analysis, using electrons of 8 eV energy, and low-energy argon ions to prevent any localized charge build-up. Data acquisition and processing using the Thermo Avantage software is described elsewhere.[33] The spectra were fitted with one or more Voigt profiles (BE uncertainty: ± 0.2 eV) and Scofield sensitivity factors were applied for quantification.[34] All spectra were referenced to the C 1s

graphitic peak at 284.4 eV binding energy controlled by means of the well-known photoelectron peaks of Cu, Ag and Au respectively. X-ray absorption near edge structure (XANES) measurements were carried out at PETRA-III beamline P65 at DESY in Hamburg and recorded in quick-XAS (7 min/spectrum) mode in fluorescence geometry using a PIPS diode. The Mn K-edge of MnO_2@rGO was measured at room temperature with a Si (111) crystal monochromator. The energy was calibrated by the absorption edge of a Mn foil, which was measured in parallel with other samples. Standard materials were MnO, Mn_2O_3, and MnO_2. The XAS spectra were processed with the DEMETER software package.[35] To further characterize further the morphology and structure of the samples, transmission electron microscopy was employed. Sample preparation for TEM consisted in the dispersion of the sample in high purity ethanol and depositing a droplet on a carbon-coated gold grid. The TEM analysis was performed on a Titan 80–300 electron microscope (FEI), equipped with a CEOS image aberration corrector, high angle annular dark field (HAADF) and a scanning transmission electron microscopy (STEM) detector as well as a Tridiem 863 Gatan image filter (GIF). The microscope was operated at an accelerating voltage of 300 kV. Elemental analysis measurements were carried out to determine the MnO_2 loading by inductively coupled plasma mass spectrometry (ICP-MS, 7500ce, Agilent) after MnO_2 was completely dissolved in acid.

3. RESULTS AND DISCUSSION

The obtained MnO_2@rGO sample was analyzed by SEM to investigate the morphology. SEM of the templated rGO sample (Figure 1a) clearly shows 3D multilayer structure. After MnO_2 deposition, this 3D multilayer structure is preserved (Figure 1b), assuring a high surface area to hold the discharge products. To determine the morphology, distribution and crystal structure of

the MnO_2 particles, STEM and high resolution TEM analyses were carried out. STEM image of the sample show that the MnO_2 nanoparticles have diameters smaller than 20 nm and are uniformly dispersed on the rGO surface (Figure 1c and d). For a more detailed investigation of the MnO_2@rGO composite, STEM-EDX elemental mappings (Manganese, Oxygen and Carbon) were recorded (Figure. S1a-d). The mappings confirm the uniform distribution of MnO_2 particles on the rGO surface. The HRTEM imaging presented in Figure 1e further confirms that nano-sized crystalline MnO_2 particles are grown on rGO. The uniform distribution can be attributed to the presence of reactive sites on the rGO surface, which aid the MnO_2 formation and it will be partially consumed by the chemical reaction with $KMnO_4$. Since the rGO template constrains the MnO_2 growth rate, the aggregation of MnO_2 nanoparticles is avoided. Further the low $KMnO_4$ concentration of the solution leads to a low amount of MnO_2 deposited on the rGO surface. All these factors promote the formation of the unique structure of the MnO_2@rGO composite.

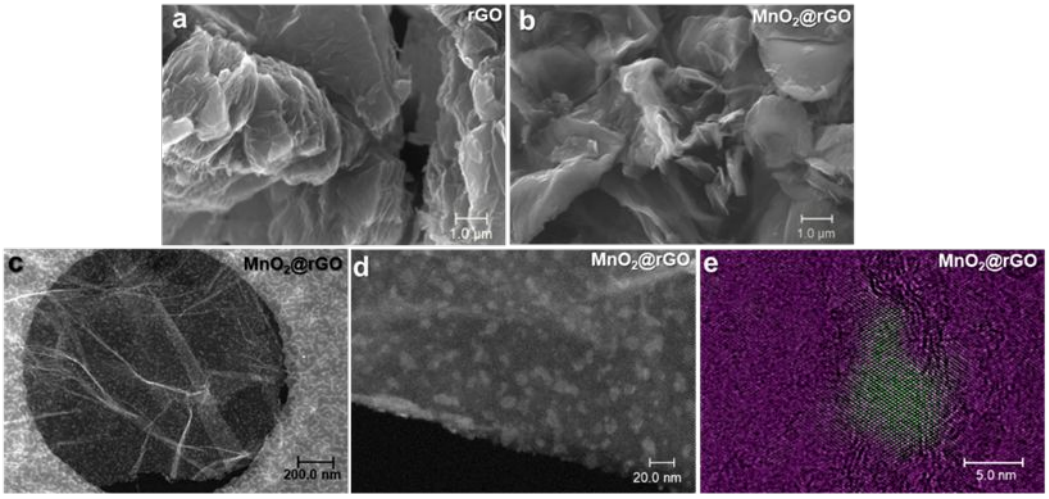

Figure 1. SEM images of raw rGO (a) and MnO_2@rGO composite (b); (c) and (d) STEM images of MnO_2@rGO; (e) Composed HRTEM image from the inverse FFT of MnO_2@rGO catalyst. The purple part is rGO substrate and the green part is MnO_2 particle.

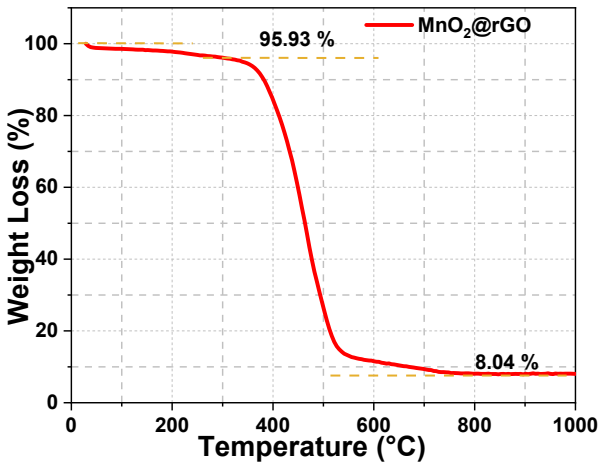

Figure 2. TG curve of MnO_2@rGO composite.

TG was used to examine the MnO_2 content of the MnO_2@rGO composite (Figure 2). A slight weight loss of about 4 wt% which occurs below 300 °C is ascribed to the removal of adsorbed and crystalline water. The followed weight loss is caused by the oxidation of rGO into CO_2 and the decomposition of MnO_2 into Mn_2O_3. Based on the residual mass of Mn_2O_3, the mass percentages of MnO_2 in MnO_2@rGO composite was estimated to ~ 9 wt%.[36] In addition to the TGA analysis, the Mn content of the MnO_2@rGO was determined to be 4.88 wt% (the content of MnO_2 was ~8 wt%) by ICP-MS analyses after dissolving the sample in 35 wt% HCl.

As shown in Figure 3, the nitrogen adsorption-desorption isotherms of rGO and MnO_2@rGO resemble a type II adsorption isotherms, which indicates a wider distribution of pore diameters.[37] The corresponding BET (Brunauer-Emmett-Teller) specific surface area for rGO and MnO_2@rGO were calculated to be 317 $m^2 g^{-1}$ and 186 $m^2 g^{-1}$. The porous structure provides sufficient space for the deposition of discharge products and facilitate the rapid transport of O_2 and Li^+.[38] Moreover, the high specific area contributes to a large catalytic active region with high number of exposed MnO_2 active sites.

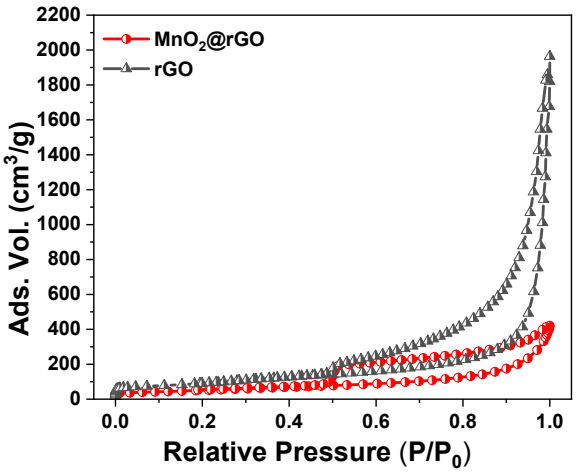

Figure 3. N_2 adsorption-desorption isotherms of rGO and MnO_2@rGO.

XRD measurements were carried out to characterize the crystallinity and phase purity of the samples. Both rGO and MnO_2@rGO samples possess two broad diffraction reflections (9.2° and 15.3°) in XRD patterns (Figure 4a). These reflections are similar to those observed for highly disordered graphitic structures. The d-spacing of the first diffraction corresponds to the (002) reflection of graphite and therefore most likely originates from small domains of stacked rGO sheets. The first diffraction position yields a mean inter graphene spacing of 0.35 nm, which is substantially larger than that of graphite (c/2 = 0.3354 nm). The XRD pattern of MnO_2@rGO shows an additional broad and weak diffraction peak at about 7.6°, which could be assigned to the (101) crystal plane of MnO_2 (JCPDS Number: 39-0375). However, due to the presence of just a single broad diffraction signal a clear crystallographic assignment is not possible. Nevertheless, the weak and broad peak confirms to the low amount of deposited manganese oxide and a rather small particle size (smaller than 20 nm).

Raman spectroscopy was applied to further investigate the structural evolution of the MnO_2@rGO, rGO and MnO_2 samples (Figure 4b). Raman spectra of MnO_2@rGO and rGO specimens both have the typical bands of carbon materials, which are located at 1335 cm^{-1} (D-band) and 1592 cm^{-1} (G-

band).[39] The two peaks are composed of four bands: D1, D3, D4 and G. The G-band is assigned to the E_{2g} phonon of sp^2-bonded carbon atoms, which is a characteristic feature of graphitic layers.[40,41] The D1-band is assigned to the breathing mode of κ-point phonons with A_{1g} symmetry, which corresponds to disordered carbon or defective graphitic structures.[40,41] The D3 peak shows the existence of fragments or functional groups in the amorphous phase which may also change the C–C and C=C stretching vibrations of the polyene-like structure (D4).[41] The area ratio of G band and D1 band (named as I_G/I_D) is generally used as an indicator for the graphitization degree of carbon materials. The I_G/I_D value is 0.37 and 0.30 for rGO and MnO_2@rGO, respectively. This indicates a rather low graphitization degree of both samples. In addition to the G-band and D-band, MnO_2@rGO sample also presents a distinct band at around 650 cm^{-1}, which corresponds to the symmetric stretching vibration M-O of [MnO_6] groups.[42]

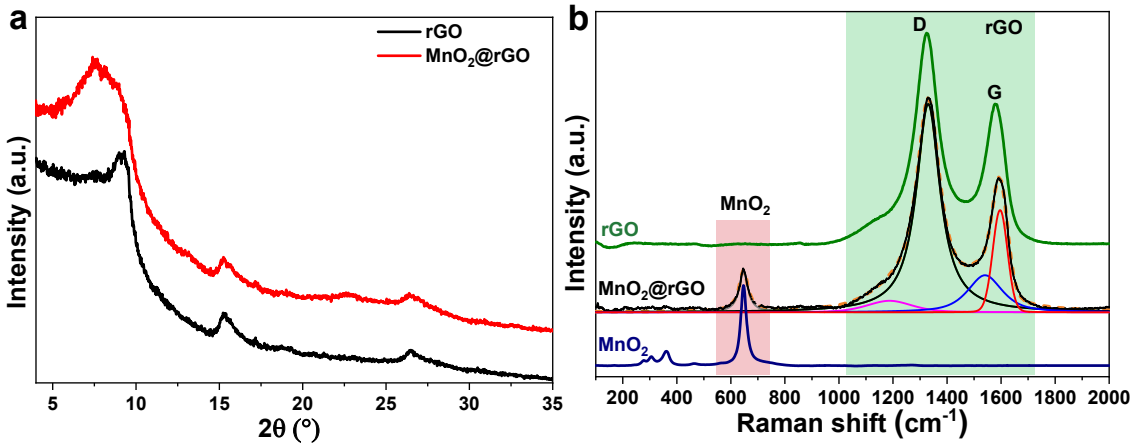

Figure 4. (a) XRD (λ=0.559407Å) patterns of rGO and MnO_2@rGO. (b) Raman spectra of rGO, MnO_2 and MnO_2@rGO.

XPS analysis was applied to determine the oxidation state and elemental composition of the prepared MnO_2@rGO. Figure. S2 shows a survey scan of MnO_2@rGO which verifies the presence of the elements Mn, O and C. The high-resolution Mn 3s spectrum shows two peaks with a separation of 5.2 eV due to spin-orbit splitting (Figure 5a). This value lies between the spin-orbit

splitting for Mn^{4+} and Mn^{3+} of 4.6 and 5.5 eV, respectively, indicating the presence of both oxidation states. The high-resolution Mn $2p_{3/2}$ spectrum was further explored to confirm this conclusion (Figure 5b). The absence of a shake-up satellite, which is typical for Mn^{2+} at ~ 646 eV, confirms the absence of Mn^{2+} in the sample. The multiplet fitting approach of Biesinger et al. was applied here and adapted as in the work of Azmi et al.[43,44] Two multiplets could be evidenced, which supports the presence of manganese in the oxidation state of Mn^{4+} and Mn^{3+} with a slightly higher concentration of Mn^{3+} (Mn^{3+}:Mn^{4+} = 3:2).

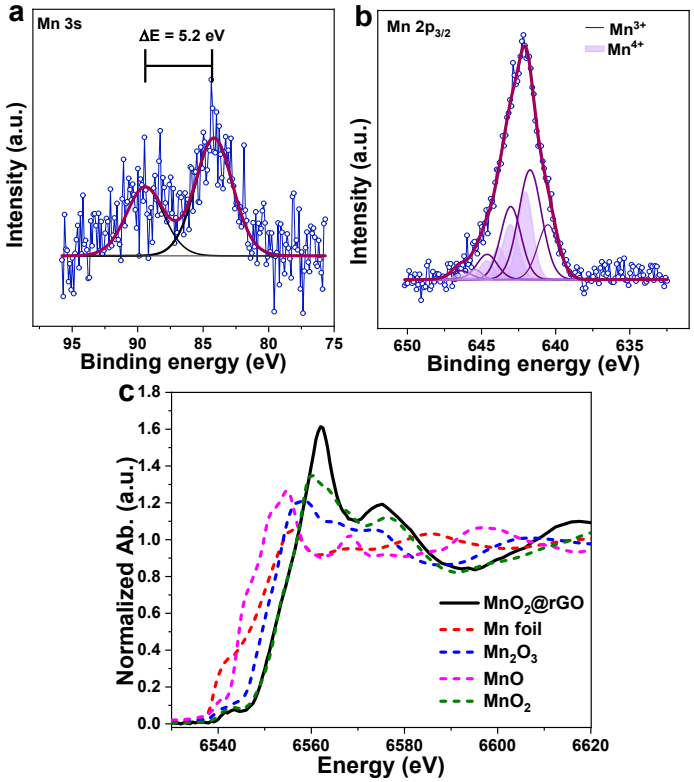

Figure 5. High-resolution Mn 3s (a) and Mn $2p_{3/2}$ (b) XPS spectra for MnO_2@rGO; (c) Normalized Mn K-edge XANES spectra of the obtained MnO_2@rGO materials together with reference spectra of Mn foil, MnO, Mn_2O_3 and MnO_2.

Since the information depth for XPS is only a few nanometers, we employed XANES spectroscopy to obtain more detailed information about the electronic structure of the bulk. Mn K-edge position of the MnO_2@rGO composite overlaps with that of standard MnO_2 (Figure 5c), which indicates

that the oxidation state of Mn in the composite is mainly Mn^{4+}. Combining the information of the XPS and XANES measurements it can be concluded that Mn^{3+} and hence oxygen vacancies are mostly enriched on the MnO_2 particle surface.

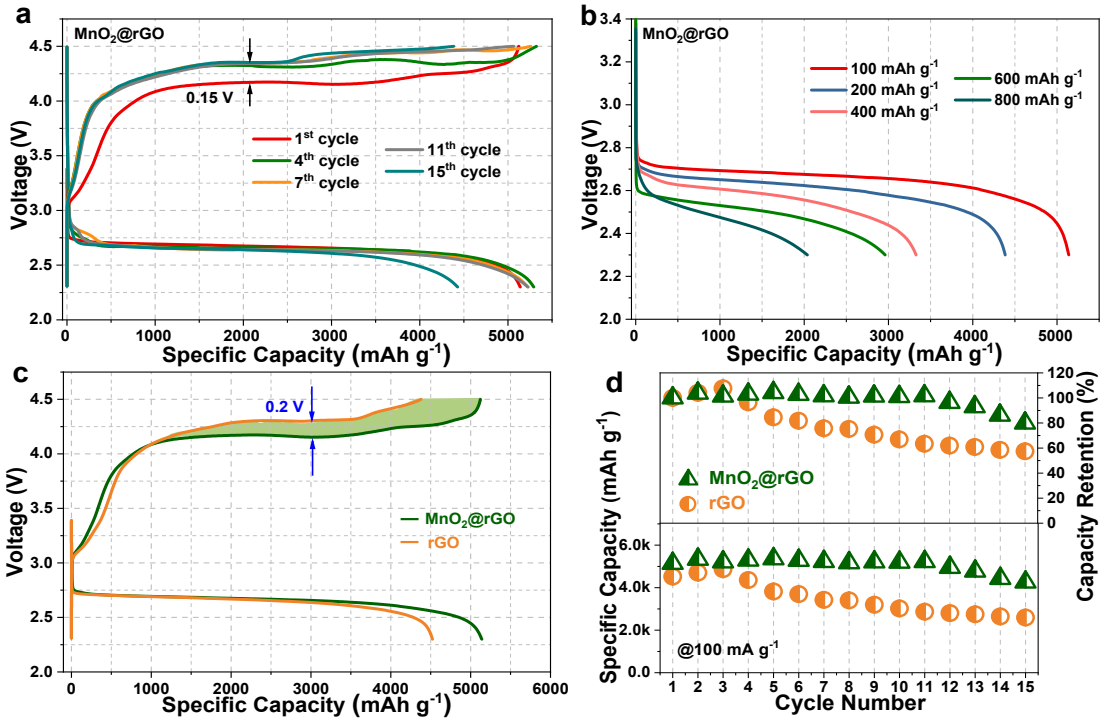

Figure 6. Galvanostatic discharge-charge curves of MnO_2@rGO (a), (b) Galvanostatic discharge curves of the MnO_2@rGO cathode at current densities from 100 to 800 mA g^{-1}; (c) Comparison of the initial discharge-charge profiles of MnO_2@rGO and rGO; (d) Variation of discharge capacity and capacity retention with cycle number for MnO_2@rGO and rGO;

Galvanostatic discharge-charge measurements were carried out to investigate the catalytic effect of the MnO_2@rGO composite. rGO and MnO_2@rGO based batteries were operated in a voltage range of 2.3-4.5 V vs. Li^+ /Li at a current of 100 mA g^{-1} for 15 full cycles (Figure 6a and S3). The MnO_2@rGO based battery exhibits a very good reversibility with almost no capacity decay within the initial 11 cycles. The charging voltage of the MnO_2@rGO based battery increases by about 0.15 V from the first to the fourth cycle. Then it stays stable for the following 11 cycles. In contrast,

the rGO based battery shows poor capacity retention with a continuous decay after the first cycle. Also the charging voltage of the rGO based battery continues to increase from the first to the fifteenth cycle. Moreover, the presence of trace water leads to an increase of discharge capacity for the MnO_2@rGO based battery (Figure. S4.) Meanwhile, the discharge voltage plateau is also slightly increased. This is because water is a strong Lewis acid and increases the solubility of LiO_2 in the electrolyte solution.[31] Therefore, the surface mechanism for the formation of discharge products is converted into a solution based mechanism.[31] To test the rate capability galvanotatic cycling experiment at current densities from 100-800 mAh g^{-1} where carried out (Figure 6b). The discharge capacity of the MnO_2@rGO based battery decreases with the cycling rate but is still capable to deliver a fairly high discharge capacity of 2025 mA h g^{-1} at a current density of 800 mA g^{-1}.

The voltage profiles during the first discharge-charge of the rGO and MnO_2@rGO based Li-O_2 batteries are displayed in Figure 6c. The MnO_2@rGO based Li-O_2 battery shows a 0.2 V lower charge voltage compared to the rGO based battery. Hence, the lower charge voltage can be attributed to the catalytic effect of MnO_2 for the OER process.[7,45] The MnO_2@rGO based battery delivers an initial discharge capacity of 5139 mAh g^{-1}. Even after the fifteenth cycle a discharge capacity of 4262 mAh g^{-1} is still obtained (Figure 6d). This corresponds to a capacity retention of about 80% after 15 cycles.

When compared to some selected important works related to the use of metal/metal oxide catalysts in Li-O_2 batteries, MnO_2@rGO exhibits a higher discharge capacity or capacity retention (Table 1) although it has a much lower catalyst content loading. For instance, in comparison to the NiO/rGO composite described by H. Wang et al, which has a similar catalyst content, our

MnO_2@rGO based battery presents much higher capacity (~4 times higher) and capacity retention.[27] There are also some reported works (MnO_2/HPC, δ-MnO_2@MWCNTs and Fe_2O_3/CNT) showing better performance.[21,46,47] However, the catalyst content of these materials (46, 34, and 75% wt%) is much higher than that of our material (9 wt%). In addition, the synthesis process of the HPC (hierarchically porous carbon) template is complex, and the electrolyte used in the work about the δ-MnO_2@MWCNTs based Li-O_2 battery is special and complex.[21,46] The Fe_2O_3/CNT based Li-O_2 batteries present longer cycle life and higher capacity retention, but the capacity is much lower than that of our battery (4~5 times lower).[47] The pure rGO based battery presents a maximum discharge capacity of 4866 mAh g^{-1} and a discharge capacity of 2597 mAh g^{-1} (53% capacity retention) after 15 cycles (Figure 6d). This value is much lower than the capacity retention of the MnO_2@rGO based battery. This demonstrates that the MnO_2 nanoparticles effectively support the OER and hence restrain the accumulation of discharge products at the electrode surface. The good catalytic activity of the MnO_2 particles may be attributed to their small particle size and high number of oxygen vacancies at their surface.

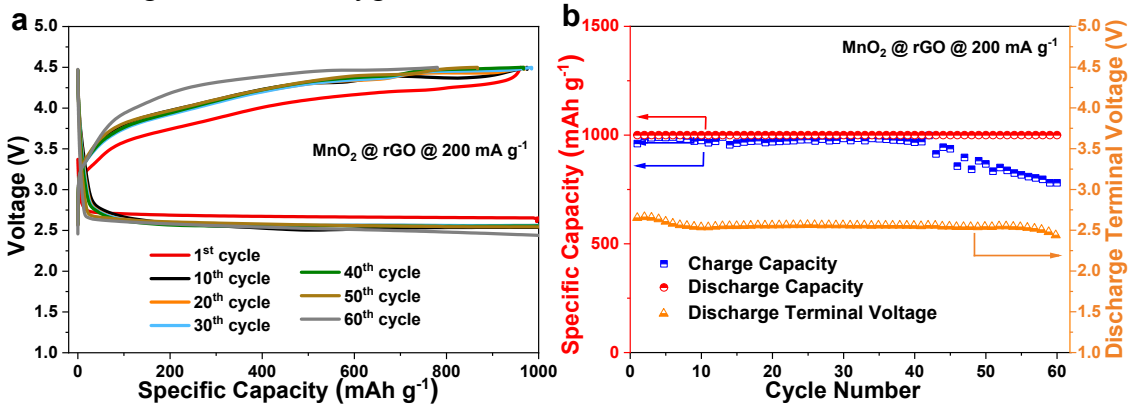

Figure 7. (a) Charge and discharge profiles of MnO_2@rGO at the 1st, 10th, 20th, 30th, 40th, 50th and 60th cycles with a specific capacity limit of 1000 mAh g^{-1} at a current density of 200 mA g^{-1}. (b) Discharge/charge capacity and discharge terminal voltage vs. cycle number at a current density of 200 mA g^{-1}.

Table 1. Selected works related to the use of Metal/Metal oxides as catalysts in Li-O_2 cells.

Catalysts	Content (wt%)	Electrolyte	Initial capacity (mAh $g^{-1}_{cathode}$)	Cycle Num.	End capacity (mAh $g^{-1}_{cathode}$)	Capacity retention (%)	Ref.
NiO/rGO	8	1 M LiTFSI in TEGDME	1023	10	697	68	27
MnO_2/HPC	46	1 M LiTFSI in TEGDME	5000	60	2000	40	21
MoSSe	100	1 M $LiClO_4$ in DMSO	708	30	725	102	48
δ-MnO_2@ MWCNTs	34	0.8/0.5 M LiTFSI $LiNO_3$ in PYR14TFSI/DMSO	28517				46
Fe_2O_3/CNT	75	0.5 M LiTFSI in TEGDME	951	50	1295	136	47
CNF@Pt	50	1 M $LiNO_3$ in DMAc	2955	24	1138	39	49
Graphene/ α-MnO_2	50	1 M $LiPF_6$ in NMP with PeO/Al_2O_3 (0.05 M/0.01 M)	2850	10	1000	35	50
$NiCo_2O_4$	30	1 M LiTFSI in TEGDME	4386	3	3552	81	51
CoO/C	45	1 M LiTFSI in TEGDME	3132	8	1999	64	52
Co/Mn/O Nanocube	44	1 M LiTFSI in TEGDME	3836	5	2072	53	53
IrO_2/MnO_2	100	1 M $LiClO_4$ in TEGDME	2600	247	701	27	54
$CoMn_2O_4$	44	0.5 M LiTFSI in TEGDME	3255	15	1667	51	55
Mn_3O_4/RGO	80	0.1 M $LiPF_6$ in DME	2300	20	920	40	7
Low-valent Mn_3O_4/RGO	47	1 M LiTFSI in TEGDME	4500				23
C/α-MnO_2	10	1 M LiTFSI in TEGDME	1400	10	500	36	18
rGO-Ni_3Pd_7	33	0.1 M $LiPF_6$ in DMSO	2512	10	750	30	56
$CoFe_2O_4$	16	0.1 M $LiPF_6$ in DMSO	7510	10	500	7	57
rGO-$Co_{48}Pt_{52}$	33	0.5 M $LiPF_6$ in DMSO	9896	4	6000	61	58
This work	9	0.25 M LiTFSI in TEGDME	5139	15	4262	83	

The cycling stability of the MnO_2@rGO based battery was further explored by galvanostatic cycling at a current density of 200 mA g^{-1} and a cut-off capacity of 1000 mAh g^{-1}. Batteries based on MnO_2@rGO showed a constant discharge capacity over 60 cycles (Figure 7a). During the first seven cycles the discharge end voltage decays slightly from 2.65 V to 2.55 V and then keeps stable at 2.55 V until the 60th cycle (Figure 7b).

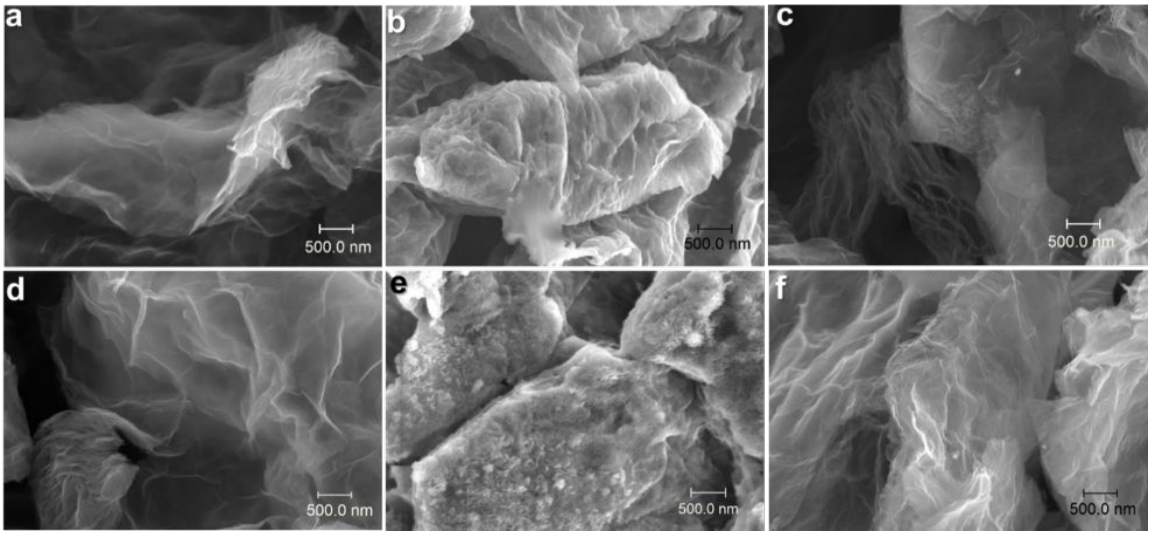

Figure 8. SEM images of pristine rGO electrode (a), after full discharge to 2.3 V (b), and recharge to 4.5 V (c); SEM images of pristine MnO_2@rGO electrode (d), after full discharge to 2.3 V (e), and recharge to 4.5 V (f);

The morphologies of the discharge products were investigated by SEM. SEM images of the pristine MnO_2@rGO electrode, after the first discharge to 2.3 V and after recharge to 4.5 V are shown in Figure 8. After discharge to 2.3 V, the porous multilayer structure of the MnO_2@rGO electrode is covered with a fine grained mossy deposition product (Figure 8e). After recharging to 4.5 V, the discharge products disappear and the original multilayer porous structure of MnO_2@rGO becomes visible again (Figure 8f). In contrast, the discharge products on the pure rGO electrode form a smooth film, which covers the electrode surface (Figure 8b). This film possibly obstructs the free transportation of electrolyte, oxygen, and electrons, leading to the

reduced capacity of pure rGO. Moreover, the discharged MnO_2@rGO electrode cycled without water shows smaller grained mossy deposits when compared to the discharge products of MnO_2@rGO cycled with trace water (Figure S5). Since O_2 supply is unlimited, the capacity limitation of Li-O_2 batteries highly depend on availability of catalytic active sites. This means that the capacity is limited by the occupation of catalytic active sites by the deposition of discharge products. Thus, the morphology of deposited discharge products during discharge is closely related to discharge capacity.[31] The very small grained mossy deposition will huddle together and leave limited space for oxygen and ion to diffuse to active sites.

Based on these SEM results, we conclude that the mass transport of LiO_2 species is enhanced by MnO_2. This enhancement may be attributed to the weakening of bindings between the intermediate (LiO_2 species) and the substrate by MnO_2.[21] Moreover, the large exposed surface of the MnO_2 nano-particles will lead to a higher interfacial current density, which reduces the reaction time to form discharged products. The enhancement of surface transport and the reduction of reaction time act together synergistically and lead to the formation of a fine grained and uniform discharge product.[21]

To identify the crystalline discharge products, XRD with Co radiation was applied. The XRD pattern clearly demonstrates that peaks corresponding to LiOH emerge after the discharge process (Figure 9b and S6). These peaks completely disappear in the subsequent charge process (Figure 9b), which indicates a complete decomposition of LiOH. Furthermore, the phase purity of the discharge products was studied by Rietveld refinement. Figure 9a confirms that the main reflections are in good agreement with the tetragonal phase of LiOH (space group: P4/nmm (129)). Satisfactory agreement factors (R_{wp} = 2.4%, R_p = 1.7%) with the cell parameter $a = b$ = 3.5487(1)

Å, c = 4.3511(1) Å, $\alpha = \beta = \gamma$ =90°, and cell volume = 54.795(3) Å^3 are determined in this crystal refinement.

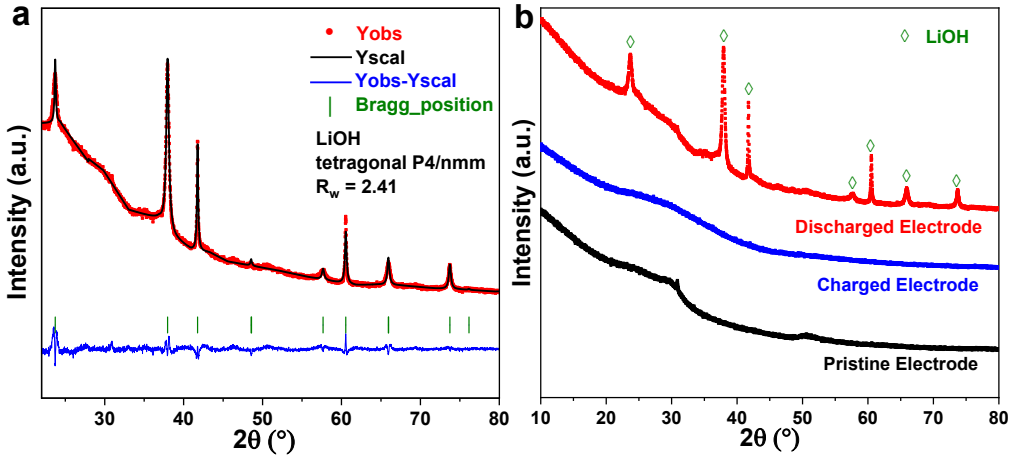

Figure 9. Rietveld refinement of the proposed LiOH structure model based on the XRD (λ=1.78896 Å) of discharged MnO_2@rGO electrode (a), XRD patterns of pristine MnO_2@rGO electrode, after discharge to 2.3 V and recharge to 4.5 V (b).

To further elucidate the nature of the discharge products, Raman measurements were carried out. The pristine electrode shows only the characteristic bands of rGO and MnO_2. After discharge to 2.3 V the appearance of new bands indicates the formation of discharge products (Figure 10a). These bands disappear again after charge (Figure 10a), indicating a reversible and almost complete decomposition of the discharge products. Most changes in the Raman spectrum of the discharged electrode occur in the range between 300 and 750 cm^{-1}. Despite some overlap, seven different bands labeled A, B, C, D, E, F and G can be distinguished in the enlarged view of this region (Figure 10b). The frequencies of the six bands labeled as B, C, D, E, F and G in Figure 10b are located at about 407, 431, 501, 566, 610 and 650 cm^{-1}, which agrees well with the vibrational bands of Li_2MnO_3.[59,60] Given the rather strong intensity of the Li_2MnO_3 bands if compared to the pristine sample and the small size of the original MnO_2 particles, it seems most likely that MnO_2 transforms into a lithiated manganese oxide during discharge. The Raman spectrum of the charged

electrode reveals that this lithiated manganese oxide is transformed back into MnO_2 again during charge. This transition between lithiated and non-lithiated manganese oxide may therefore at least be partially responsible for the catalytic activity of MnO_2 in Li-O_2 batteries by reducing the electron transfer resistance and O_2 desorption energy.[61] The discharged electrode also shows another prominent band (labeled as A) at 320 cm^{-1} which can be attributed to LiOH (Figure 9b) based on referenc e measurements (Figure S7).

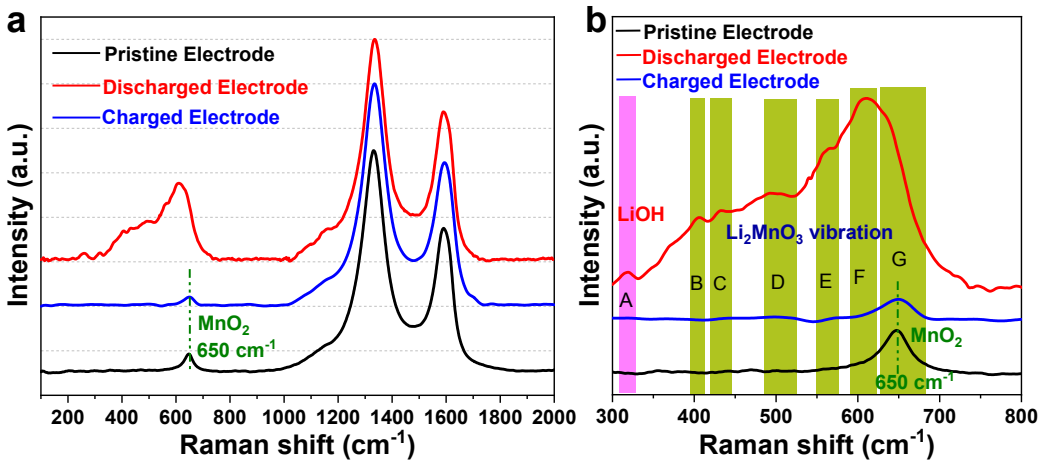

Figure 10. Raman spectra of pristine MnO_2@rGO electrode, after discharge to 2.3 V and recharge to 4.5 V (a). (b) The magnified Raman spectra in the range 300-800 cm^{-1} of pristine MnO_2@rGO electrode, after discharge to 2.3 V and recharge to 4.5 V.

As outlined above, the Raman spectrum from rGO exhibits two distinct peaks located at 1335 cm^{-1} (D-bands) and 1592 cm^{-1} (G-bands). To study changes of the rGO during the discharge and charge process the Raman spectra in the range between 800-2000 cm^{-1} were deconvoluted into four component bands (D1, D3, D4 and G) (Figure S8). I_{D3}/I_T values were calculated from the area ratio of D3 band and the total integral intensity of all four bands (I_T). This ratio reflects the amount of fragments or functional groups in amorphous phases.[62] I_{D3}/I_T values for both rGO and MnO_2@rGO electrodes increase after discharge. This indicates an increase of fragments or functional groups in the amorphous phase, which is ascribed to the side reactions during battery

cycling with the electrolyte or the rGO itself. It can be seen that I_{D3}/I_T value of rGO electrode increases much more than that of the MnO_2@rGO electrode, indicating more side reactions for the rGO electrode. After charge, the I_{D3}/I_T value of MnO_2@rGO electrode decreases back to 0.12, which indicates an almost complete removal of side products from electrode surface. In contrast, the I_{D3}/I_T value of rGO electrode after charge (0.14) stays elevated compared to its initial value (0.11). This suggests an incomplete removal of side products in case of the rGO electrode, which will result in a gradual accumulation of side products on the oxygen electrode and early cell death.

4. CONCLUSION

An MnO_2@rGO composite with a low amount of nano-sized MnO_2 (9 wt%) uniformly deposited on the rGO surface has been synthesized and was investigated as oxygen electrode for Li-O_2 batteries. Though the amount of MnO_2 is very low in the composite, the composite still possesses a high catalytic activity. Batteries catalyzed by MnO_2@rGO delivered an initial discharge capacity of 5139 mAh g^{-1} and retained about 80% of their capacity (4262 mAh g^{-1}) after 15 full discharge-charge cycles at a current density of 100 mA g^{-1}. Moreover, the charge voltage is reduced by 0.2 V compared to pure rGO based battery. The remarkable improvement of the electrochemical performance is due to the unique structure of MnO_2@rGO and the strong synergistic effect between the nanosized MnO_2 particles and the rGO support. Firstly, the high rGO content assures a good electron conductivity, which facilitates electron transfer. Secondly, the 3D porous graphene frameworks made of multiple layers provides a matrix with high surface area for the deposition of discharge products. Thirdly, the porous structure also promises good transport properties for ionic and oxygen diffusion inside the electrode. Fourthly, the nano-sized MnO_2 (smaller than 20 nm) improves the catalytic activity of the surface which leads to higher interfacial current densities and

shorter reaction times. Further, the surface transport of Li_xO_2 species is enhanced by MnO_2. Both aspects contribute to the formation of a thin film of uniformly distributed discharged products of small particle size, which can be easily decomposed during charge. Further, we found evidence for the reversible transition of manganese oxide into lithiated manganese oxide during discharge. This transition, which involves the incorporation of lithium and oxygen, seems to play an important role for the catalytic activity of MnO_2 and hence the reduction of the electron transfer resistance of the OER.

ASSOCIATED CONTENT

Supporting Information.

The following files are available free of charge.

STEM and the corresponding elemental mapping of Manganese, Oxygen and Carbon images of the MnO_2@rGO. XPS survey spectrum of the MnO_2@rGO. Galvanostatic discharge-charge curves of rGO cycled at a current density of 100 mA g^{-1} between 2.3 V-4.5 V. Galvanostatic discharge-charge curves of MnO_2@rGO cycled without water at a current density of 100 mA g^{-1} between 2.3 V-4.5 V. SEM images of MnO_2@rGO electrode after full discharge to 2.3 V with no water. XRD spectra of rGO electrode after discharge to 2.3 V. Raman spectra of raw LiOH. Deconvoluted Raman spectra of the pristine MnO_2@rGO electrode, after discharge to 2.3 V and recharge to 4.5 V (PDF).

AUTHOR INFORMATION

Corresponding Author

*E-mail address: frieder.scheiba@kit.edu (F. Scheiba); Tel.:+49 721 608 28506

Notes

There are no conflicts to declare.

ACKNOWLEDGMENT

This work was supported by the China Scholarship Council (CSC grant number: 20159969613). The work also got technical support from Udo Geckle (SEM measurement) and Dr. Dominique Mook (N_2 adsorption and desorption isotherms). We acknowledge the Deutsche Elektronen-Syncrotron (DESY) in Hamburg, Germany, for provision of beam-time at the P65 beamline of the synchrotron radiation source Petra-III. We would like to thank Edmund Welter from Experiments Division in DESY, Hamburg. We acknowledge the KNMF for the provision of TEM and ICP-MS measurements. This work contributes to the research performed at CELEST (Center for Electrochemical Energy Storage Ulm-Karlsruhe).

REFERENCES

(1) Liu, T.; Leskes, M.; Yu, W.; Moore, A. J.; Zhou, L.; Bayley, P. M.; Kim, G.; Grey, C. P. Cycling Li-O_2 Batteries via LiOH Formation and Decomposition. *Science* **2015**, *350*, 530-533.

(2) Zhao, G.; Mo, R.; Wang, B.; Zhang, L.; Sun, K. Enhanced Cyclability of Li-O_2 Batteries Based on TiO_2 Supported Cathodes with No Carbon or Binder. *Chem. Mater.* **2014**, *26*, 2551-2556.

(3) Xu, J.-J.; Wang, Z.-L.; Xu, D.; Meng, F.-Z.; Zhang, X.-B. 3D Ordered Macroporous $LaFeO_3$ as Efficient Electrocatalyst for Li-O_2 Batteries with Enhanced Rate Capability and Cyclic Performance. *Energy Environ. Sci.* **2014**, *7* (7), 2213.

(4) Ding, N.; Chien, S. W.; Hor, T. S. A.; Lum, R.; Zong, Y.; Liu, Z. Influence of Carbon Pore Size on the Discharge Capacity of Li-O_2 Batteries. *J. Mater. Chem. A* **2014**, *2* (31), 12433-12441.

(5) Oh, S. H.; Black, R.; Pomerantseva, E.; Lee, J. H.; Nazar, L. F. Synthesis of a Metallic Mesoporous Pyrochlore as a Catalyst for Lithium-O_2 Batteries. *Nat. Chem.* **2012**, *4* (12), 1004-1010.

(6) Guo, Z.; Zhou, D.; Dong, X.; Qiu, Z.; Wang, Y.; Xia, Y. Ordered Hierarchical Mesoporous/Macroporous Carbon: A High-Performance Catalyst for Rechargeable Li-O_2 Batteries. *Adv. Mater.* **2013**, *25* (39), 5668-5672.

(7) Li, Q.; Xu, P.; Zhang, B.; Tsai, H.; Wang, J.; Wang, H.-L.; Wu, G. One-Step Synthesis of Mn_3O_4/Reduced Graphene Oxide Nanocomposites for Oxygen Reduction in Nonaqueous Li-O_2 Batteries. *Chem. Commun.* **2013**, *49* (92), 10838.

(8) Zhu, L.; Gao, Q.; Tan, Y.; Tian, W.; Xu, J.; Yang, K.; Yang, C. Nitrogen and Oxygen Co-Doped Microporous Carbons Derived from the Leaves of Euonymus Japonicas as High Performance Supercapacitor Electrode Material. *Micropor. Mesopor. Mater.* **2015**, *210*, 1-9.

(9) Zeng, F.; Pan, Y.; Yang, Y.; Li, Q.; Li, G.; Hou, Z.; Gu, G. Facile Construction of Mn_3O_4-MnO_2 hetero-Nanorods/Graphene Nanocomposite for Highly Sensitive Electrochemical Detection of Hydrogen Peroxide. *Electrochim. Acta* **2016**, *196*, 587-596.

(10) Lu, Y.-C.; Gasteiger, H. A.; Crumlin, E.; McGuire, R.; Shao-Horn, Y. Electrocatalytic Activity Studies of Select Metal Surfaces and Implications in Li-Air Batteries. *J.*

Electrochem. Soc. **2010**, *157* (9), A1016–A1025.

(11) Ryu, W. H.; Yoon, T. H.; Song, S. H.; Jeon, S.; Park, Y. J.; Kim, I. D. Bifunctional Composite Catalysts Using Co_3O_4 Nanofibers Immobilized on Nonoxidized Graphene Nanoflakes for High-Capacity and Long-Cycle Li-O_2 Battery. *Nano Lett.* **2013**, *13* (9), 4190-4197.

(12) Lei, Y.; Lu, J.; Luo, X.; Wu, T.; Du, P.; Zhang, X.; Ren, Y.; Wen, J.; Miller, D. J.; Miller, J. T. Synthesis of Porous Carbon Supported Palladium Nanoparticle Catalysts by Atomic Layer Deposition: Application for Rechargeable Lithium-O_2 Battery. *Nano Lett.* **2013**, *13* (9), 4182-4189.

(13) Xu, J.-J.; Xu, D.; Wang, Z.-L.; Wang, H.-G.; Zhang, L.-L.; Zhang, X.-B. Synthesis of Perovskite-Based Porous $La_{0.75}Sr_{0.25}MnO_3$ Nanotubes as a Highly Efficient Electrocatalyst for Rechargeable Lithium-Oxygen Batteries. *Angew. Chem. Int. Ed.* **2013**, *52* (14), 3887-3890.

(14) Lu, X.; Zhang, L.; Sun, X.; Si, W.; Yan, C.; Schmidt, O. G. Bifunctional Au-Pd Decorated MnO_x Nanomembranes as Cathode Materials for Li-O_2 Batteries. *J. Mater. Chem. A* **2016**, *4* (11), 4155-4160.

(15) Sun, N.; Liu, H.; Yu, Z.; Zheng, Z.; Shao, C. Mn-Doped $La_{0.6}Sr_{0.4}CoO_3$ perovskite Catalysts with Enhanced Performances for Non-Aqueous Electrolyte Li-O_2 Batteries. *RSC Adv.* **2016**, *6* (16), 13522-13530.

(16) Cao, Y.; Wei, Z.; He, J.; Zang, J.; Zhang, Q.; Zheng, M.; Dong, Q. α-MnO_2 nanorods Grown in Situ on Graphene as Catalysts for Li-O_2 Batteries with Excellent Electrochemical

Performance. *Energy Environ. Sci.* **2012**, *5* (12), 9765-9768.

(17) Han, X.; Hu, Y.; Yang, J.; Cheng, F.; Chen, J. Porous Perovskite $CaMnO_3$ as an Electrocatalyst for Rechargeable Li-O_2 Batteries. *Chem. Commun.* **2014**, *50* (12), 1497–1499.

(18) Qin, Y.; Lu, J.; Du, P.; Chen, Z.; Ren, Y.; Wu, T.; Miller, J. T.; Wen, J.; Miller, D. J.; Zhang, Z. In Situ Fabrication of Porous-Carbon-Supported α-MnO_2 Nanorods at Room Temperature: Application for Rechargeable Li-O_2 Batteries. *Energy Environ. Sci.* **2013**, *6* (2), 519-531.

(19) Wang, H.; Yang, Y.; Liang, Y.; Zheng, G.; Li, Y.; Cui, Y.; Dai, H. Rechargeable Li-O_2 Batteries with a Covalently Coupled $MnCo_2O_4$-Graphene Hybrid as an Oxygen Cathode Catalyst. *Energy Environ. Sci.* **2012**, *5* (7), 7931-7935.

(20) Elmacı, G.; Ertürk, A. S.; Sevim, M.; Metin, Ö. MnO_2 Nanowires Anchored on Mesoporous Graphitic Carbon Nitride (MnO_2@mpg-C_3N_4) as a Highly Efficient Electrocatalyst for the Oxygen Evolution Reaction. *Int. J. Hydrogen Energy* **2019**, *4*.

(21) Han, X.; Cheng, F.; Chen, C.; Hu, Y.; Chen, J. Uniform MnO2 Nanostructures Supported on Hierarchically Porous Carbon as Efficient Electrocatalysts for Rechargeable Li-O_2 Batteries. *Nano Res.* **2014**, *8* (1), 156–164.

(22) Gu, T.; Agyeman, D. A.; Shin, S.; Jin, X.; Lee, J. M. A -MnO_2 Nanowire-Anchored Highly Oxidized Cluster as a Catalyst for Li-O_2 Batteries : Superior Electrocatalytic Activity and High Functionality. *Angew. Chem. Int. Ed.* **2018**, *57*, 15984–15989.

(23) Adpakpang, K.; Oh, S. M.; Agyeman, D. A.; Jin, X. Holey 2D Nanosheets of Low-Valent Manganese Oxides with an Excellent Oxygen Catalytic Activity and a High Functionality as a Catalyst for Li-O_2 Batteries. *Adv. Funct. Mater.* **2018**, *28*, 1707106.

(24) Bi, R.; Liu, G.; Zeng, C.; Wang, X.; Zhang, L.; Qiao, S. 3D Hollow α -MnO_2 Framework as an Efficient Electrocatalyst for Lithium-Oxygen Batteries. *Small* **2019**, *4*, 1804958.

(25) Jian, Z.; Liu, P.; Li, F.; He, P.; Guo, X.; Chen, M.; Zhou, H. Core-Shell-Structured CNT@RuO_2 Composite as a High-Performance Cathode Catalyst for Rechargeable Li-O_2 Batteries. *Angew. Chem. Int. Ed.* **2014**, *53* (2), 442–446.

(26) Gao, R.; Yang, Z.; Zheng, L.; Gu, L.; Liu, L.; Lee, Y. L.; Hu, Z.; Liu, X. Enhancing the Catalytic Activity of Co_3O_4 for Li-O_2 Battery through the Synergy of Surface/Interface/Doping Engineering. *ACS Catal.* **2018**, *8*, 1955–1963.

(27) Wang, H. Q.; Fan, X. P.; Zhang, X. H.; Huang, Y. G.; Wu, Q.; Pan, Q. C.; Li, Q. Y. In Situ Growth of NiO Nanoparticles on Carbon Paper as a Cathode for Rechargeable Li-O_2 Batteries. *RSC Adv.* **2017**, *7* (38), 23328-23333.

(28) Yang, C.; Gao, Q.; Tian, W.; Tan, Y.; Zhang, T.; Yang, K.; Zhu, L. Superlow Load of Nanosized MnO on a Porous Carbon Matrix from Wood Fi Bre with Superior Lithium Ion Storage Performance. *J. Mater. Chem. A* **2014**, *2*, 19975-19982.

(29) Black, R.; Lee, J. H.; Adams, B.; Mims, C. a.; Nazar, L. F. The Role of Catalysts and Peroxide Oxidation in Lithium-Oxygen Batteries. *Angew. Chem. Int. Ed.* **2013**, *52* (1), 392-396.

(30) Meini, S.; Piana, M.; Tsiouvaras, N.; Garsuch, A.; Gasteiger, H. A. The Effect of Water on the Discharge Capacity of a Non-Catalyzed Carbon Cathode for Li-O_2 Batteries. *Electrochem. Solid State Lett. 15* (4), A45-A48.

(31) Aetukuri, N. B.; McCloskey, B. D.; Garciá, J. M.; Krupp, L. E.; Viswanathan, V.; Luntz, A. C. Solvating Additives Drive Solution-Mediated Electrochemistry and Enhance Toroid Growth in Non-Aqueous Li-O_2 Batteries. *Nat. Chem.* **2015**, *7* (1), 50-56.

(32) Tellgren, R. Neutron Powder Diffraction in Sweden. *Phys. B* **1985**, *26 A*, 55-69.

(33) K. L. Parry, A. G. Shard, R. D. Short, R. G. White, J. D. W. and A. W. ARXPS Characterisation of Plasma Polymerised Surface Chemical Gradients. *Surf. Interface Anal.* **2006**, *38* (August), 1497-1504.

(34) Scofield, J. H. HARTREE-SLATER SUBSHELL PHOTOIONIZATION CROSS-SECTIONS AT 1254 AND 1487 EV. *J. EIectron Spectrosc.* **1976**, *8*, 129-137.

(35) Ravel, B.; Newville, M. ATHENA, ARTEMIS, HEPHAESTUS: Data Analysis for X-Ray Absorption Spectroscopy Using IFEFFIT. *J. Synchrotron Rad.* **2005**, *12* (4), 537-541.

(36) Xin, G.; Wang, Y.; Zhang, J.; Jia, S.; Zang, J.; Wang, Y. A Self-Supporting Graphene/MnO_2 Composite for High-Performance Supercapacitors. *Int. J. Hydrogen Energy.* **2015**, *40* (32), 10176-10184.

(37) Zhao, C. T.; Yu, C.; Liu, S. H.; Yang, J.; Fan, X. M.; Huang, H. W.; Qiu, J. 3D Porous N-Doped Graphene Frameworks Made of Interconnected Nanocages for Ultrahigh-Rate and Long-Life Li-O_2 Batteries. *Adv. Funct. Mater.* **2015**, *25* (44), 6913-6920.

(38) Zhang, S.; Wen, Z.; Lu, Y.; Wu, X.; Yang, J. Highly Active Mixed-Valent MnO_x Spheres Constructed by Nanocrystals as Efficient Catalysts for Long-Cycle Li-O_2 Batteries. *J. Mater. Chem. A* **2016**, *4*, 17129-17137.

(39) Tian, W.; Gao, Q.; Tan, Y.; Zhang, Y.; Xu, J.; Li, Z.; Yang, K.; Zhu, L.; Liu, Z. Three-Dimensional Functionalized Graphenes with Systematical Control over the Interconnected Pores and Surface Functional Groups for High Energy Performance Supercapacitors. *Carbon* **2015**, *85*, 351-362.

(40) Dresselhaus, M. S.; Dresselhaus, G.; Saito, R.; Jorio, A. Raman Spectroscopy of Carbon Nanotubes. *Phys. Rep.* **2005**, *409* (2), 47-49.

(41) Ferrari, A. C. Raman Spectroscopy of Graphene and Graphite: Disorder, Electron-Phonon Coupling, Doping and Nonadiabatic Effects. *Solid State Commun.* **2007**, *143* (1–2), 47-57.

(42) Wang, Y.; Guan, H.; Du, S.; Wang, Y. A Facile Hydrothermal Synthesis of MnO_2 Nanorod-Reduced Graphene Oxide Nanocomposites Possessing Excellent Microwave Absorption Properties. *RSC Adv.* **2015**, *5* (108), 88979-88988.

(43) Azmi, R.; Ulrich, S. Surface Analytical Approaches to Reliably Characterize Lithium Ion Battery Electrodes. *Surf Interface Anal.* **2017**, *50* (September), 43-51.

(44) Biesinger, M. C.; Payne, B. P.; Grosvenor, A. P.; Lau, L. W. M.; Gerson, A. R.; St, R.; Smart, C. Resolving Surface Chemical States in XPS Analysis of First Row Transition Metals , Oxides and Hydroxides : Cr , Mn , Fe , Co and Ni. *Appl. Surf. Sci.* **2011**, *257*, 2717-2730.

(45) Wang, F.; Wen, Z.; Shen, C.; Wu, X.; Liu, J. Synthesis of α-MnO_2 Nanowires Modified by Co_3O_4 Nanoparticles as a High-Performance Catalyst for Rechargeable Li-O_2 Batteries. *Phys. Chem. Chem. Phys.* **2016**, *18* (2), 926-931.

(46) Ma, L.; Meng, N.; Zhang, Y.; Lian, F. Improved Electrocatalytic Activity of δ -MnO_2@ MWCNTs by Inducing the Oriented Growth of Oxygen Reduction Products in Li-O_2 Batteries. *Nano Energy* **2019**, *58* (December 2018), 508-516.

(47) Li, Z.; Ganapathy, S.; Xu, Y.; Zhu, Q.; Chen, W.; Kochetkov, I.; George, C.; Nazar, L. F.; Wagemaker, M. Fe_2O_3 Nanoparticle Seed Catalysts Enhance Cyclability on Deep (Dis)Charge in Aprotic Li_2O_2 Batteries. *Adv. Energy Mater.* **2018**, *8*, 1703513.

(48) Zhang, S.; Huang, Z.; Wen, Z.; Zhang, L.; Jin, J.; Shahbazian-Yassar, R.; Yang, J. Local Lattice Distortion Activate Metastable Metal Sulfide as Catalyst with Stable Full Discharge-Charge Capability for Li-O_2 Batteries. *Nano Lett.* **2017**, *17* (6), 3518-3526.

(49) Bui, H. T.; Kim, D. Y.; Kim, D. W.; Suk, J.; Kang, Y. Carbon Nanofiber@platinum by a Coaxial Electrospinning and Their Improved Electrochemical Performance as a Li-O_2 Battery Cathode. *Carbon* **2018**, *130*, 94-104.

(50) Cetinkaya, T.; Akbulut, H.; Tokur, M.; Ozcan, S.; Uysal, M. High Capacity Graphene/α-MnO_2 nanocomposite Cathodes for Li-$_{O2}$ Batteries. *Int. J. Hydrogen Energy.* **2016**, *41* (23), 9746-9754.

(51) Sennu, P.; Park, H. S.; Park, K. U.; Aravindan, V.; Nahm, K. S.; Lee, Y. S. Formation of $NiCo_2O_4$ rods over Co_3O_4 nanosheets as Efficient Catalyst for Li-O_2 Batteries and Water Splitting. *J. Catal.* **2017**, *349*, 175-182.

(52) Gao, R.; Li, Z.; Zhang, X.; Zhang, J.; Hu, Z.; Liu, X. Carbon-Dotted Defective CoO with Oxygen Vacancies: A Synergetic Design of Bifunctional Cathode Catalyst for Li-O_2 Batteries. *ACS. Catal.* **2016**, *6* (1), 400-406.

(53) Zhang, J.; Wang, L.; Xu, L.; Ge, X.; Zhao, X.; Lai, M.; Liu, Z.; Chen, W. Porous Cobalt-Manganese Oxide Nanocubes Derived from Metal Organic Frameworks as a Cathode Catalyst for Rechargeable Li-O_2 Batteries. *Nanoscale* **2015**, *7* (2), 720-726.

(54) Tang, C.; Sun, P.; Xie, J.; Tang, Z.; Yang, Z.; Dong, Z. Two-Dimensional $IrO_2/_{MnO2}$ Enabling Conformal Growth of Amorphous. *Energy Storage Mater.* **2017**, *9* (July), 206-213.

(55) Sadighi, Z.; Huang, J.; Qin, L.; Yao, S.; Cui, J.; Kim, J. Positive Role of Oxygen Vacancy in Electrochemical Performance of $CoMn_2O_4$ Cathodes for Li-O_2 Batteries. *J. Power Sources* **2017**, *365*, 134-147.

(56) Sevim, M.; Şener, T.; Metin, Ö. Monodisperse MPd (M: Co, Ni, Cu) Alloy Nanoparticles Supported on Reduced Graphene Oxide as Cathode Catalysts for the Lithium-Air Battery. *Int. J. Hydrogen Energy* **2015**, *40* (34), 10876-10882.

(57) Şener, T.; Kayhan, E.; Sevim, M.; Metin, Ö. Monodisperse $CoFe_2O_4$ Nanoparticles Supported on Vulcan XC-72: High Performance Electrode Materials for Lithium-Air and Lithium-Ion Batteries. *J. Power Sources* **2015**, *288*, 36-41.

(58) Sevim, M.; Francia, C.; Amici, J.; Vankova, S.; Şener, T.; Metin, Ö. Bimetallic MPt (M: Co, Cu, Ni) Alloy Nanoparticles Assembled on Reduced Graphene Oxide as High Performance Cathode Catalysts for Rechargable Lithium-Oxygen Batteries. *J. Alloys*

Compd. **2016**, *683*, 231-240.

(59) Wu, Q.; Maroni, V. A.; Gosztola, D. J.; Miller, D. J.; Dees, D. W.; Lu, W. A Raman-Based Investigation of the Fate of Li_2MnO_3 in Lithium- and Manganese-Rich Cathode Materials for Lithium Ion Batteries. *J. Electrochem. Soc.* **2015**, *162* (7), A1255-A1264.

(60) Ramana, C. V; Massot, M.; Julien, C. M. XPS and Raman Spectroscopic Characterization of $LiMn_2O_4$ Spinels. *Surf. Interface Anal.* **2020**, *37*, 412-16.

(61) Zhu, J.; Ren, X.; Liu, J.; Zhang, W.; Wen, Z. Unraveling the Catalytic Mechanism of Co_3O_4 for the Oxygen Evolution Reaction in a Li-O_2 Battery. *ACS Catal.* **2015**, *5* (1), 73-81.

(62) Sadezky, A.; Muckenhuber, H.; Grothe, H.; Niessner, R.; Pöschl, U. Raman Microspectroscopy of Soot and Related Carbonaceous Materials: Spectral Analysis and Structural Information. *Carbon* **2005**, *43* (8), 1731-1742.

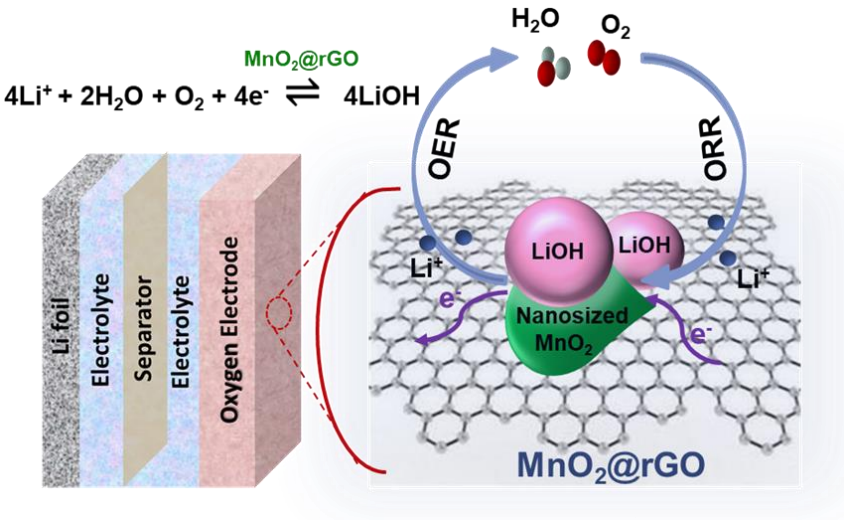
MnO2@rGO
4Li+ + 2H2O + O2 + 4e- ⇌ 4LiOH
H2O
O2
OER
ORR
Li foil
Electrolyte
Separator
Electrolyte
Oxygen Electrode
LiOH
LiOH
Li+
Li+
e-
e-
Nanosized MnO2
MnO2@rGO